



Stability of Supersonic Flow with Injection

B. E. Schmidt* and J. E. Shepherd†

California Institute of Technology, Pasadena, California 91125

DOI: 10.2514/1.J058080

Gas injection into supersonic flow past a 5° half-angle cone is studied with three injected gases: helium, nitrogen, and RC318. Experiments are performed in a Mach 4 Ludwieg tube with nitrogen as the free stream gas. The injector section is shaped to admit a “tuned” injection rate where the displacement created by injection counteracts the effects created by the injector geometry. A high-speed schlieren imaging system with a framing rate of 290 kHz is used to study the instability in the region of flow downstream of injection, referred to as the injection layer. Measurements of wavelength, convective speed, and frequency of the instability waves were made. The stability characteristics of the injection layer are found to be very similar to those of a shear layer. The findings of this work suggest that shear layer modes should be a primary concern for future stability analyses of supersonic flow with injection.

Nomenclature

a	=	sound speed, m/s
d	=	jet diameter, m
F	=	nondimensional injected mass flux
f	=	frequency, Hz
J	=	nondimensional injected momentum flux
L_{inj}	=	length of injector section, m
M	=	Mach number
n	=	optical index of refraction
\hat{Re}	=	unit Reynolds number, 1/m
Re_x	=	Reynolds number based on x
T	=	temperature, K
u	=	velocity, m/s
W	=	molar mass, g/mol
x	=	coordinate along cone surface, m
y	=	height of jet centerline, m
γ	=	ratio of specific heats
δ	=	injection layer thickness, m
λ	=	wavelength, m
ρ	=	density, kg/m ³

Subscripts

c	=	convective quantity
inj	=	injected gas quantity
j	=	jet quantity
l	=	local quantity at cone surface
ω	=	vorticity
∞	=	free stream quantity

I. Introduction

INJECTION into hypersonic boundary layers is a potential enabling technology for future high-speed vehicles. Two promising applications, localized transpiration cooling [1–5] and fuel injection in scramjet inlets [6–10], are potentially enabling technologies for future high-speed vehicles and are active areas of research. For both of these applications the stability properties of the

boundary layer downstream of the injection location, called the injection layer in this work for clarity purposes, are important. In cooling applications, the injection layer should be laminar for as great a distance as possible to maximize the extent of cooling for the protection of surface-mounted instruments on a vehicle. Marvin and Akin [4] observed that heat flux increases significantly when the injection layer transitions to turbulence as hot gas is mixed with the injected gas and transported to the wall. Conversely, in fuel injection applications, transition to turbulence is desired as it enhances mixing of reactants and leads to more chemical reactions and production of radicals. Barth et al. [10] showed that, when this occurs in scramjet inlets, efficiency of the scramjet engine system is increased.

Although the stability of the injection layer is of great importance in this flow, relatively few studies have been performed to characterize its stability properties. The majority of experimental data pertaining to the stability of this flow consist of measurements of transition location [11]. Although these data are valuable, they contribute little to understanding the physics of the transition process or illuminate the dominant transition mechanisms. A handful of numerical studies have been performed to analyze stability of these flows (e.g., Li et al. [12]), and these works use tools developed for analyzing boundary-layer stability to characterize the dominant instability modes. Of these studies, the vast majority consider injection of the same gas as the free stream gas because they are much simpler to analyze computationally due to the decoupling of the transport equation from the Navier–Stokes equations. However, in most practical applications the injected gas would be different from the free stream gas, motivating an experimental investigation of the stability properties of supersonic flow with injection, including injection of foreign (i.e., different from the free stream) gas species.

Schmidt et al. [13] examined the stability properties through an experimental study of injection into the boundary layer on a sharp, 5° half-angle cone in Mach 4 flow. That study demonstrated that injection creates a sudden increase in the displacement thickness of the boundary layer and produces oblique waves that propagate into the free stream. The waves can be strong enough to cause the injection layer to rapidly transition to turbulence, and can lead to pressure losses in internal flows as observed by Ogawa et al. [14]. Schmidt et al. [13] found that shaping the injector can compensate for the displacement effect of injection and minimize the strength of the waves created by injection when the injection rate is suitably tuned to the geometry. Most important, a “tuned” condition exists such that the displacement effect of injection counteracts the effect of the expansion at the cone tip-injector junction. At this condition, no wave (shock or expansion) is observed at the junction between the rear of the cone tip section and the front of the injector section. Schmidt et al. [13] also investigated the stability properties of the injection layer by measuring the wavelength of the instability waves in experiments and by linear stability analysis, although that study did not consider foreign gas injection.

The current paper documents and analyzes the instability that precedes transition and the displacement effect in greater detail and

Presented as paper 2016-0599 at the 54th AIAA Aerospace Sciences Meeting, San Diego, CA, 04–08 January 2016; received 5 November 2018; revision received 15 June 2019; accepted for publication 4 July 2019; published online 5 August 2019. Copyright © 2019 by Bryan E. Schmidt and Joseph E. Shepherd. Published by the American Institute of Aeronautics and Astronautics, Inc., with permission. All requests for copying and permission to reprint should be submitted to CCC at www.copyright.com; employ the eISSN 1533-385X to initiate your request. See also AIAA Rights and Permissions www.aiaa.org/randp.

*Post-Doctoral Scholar, Mechanical and Aerospace Engineering; currently at Ohio State University, 201 W 19th Ave. Member AIAA.

†Professor, Aerospace Engineering, 1200 E California Blvd. MC 205-45. Member AIAA.

for multiple injected gases, and develops a correlating parameter for the injection rate that can predict whether the flow rate is tuned for a given injector geometry for a much wider range of injected gas molar mass than previously considered. The experiments use the same configuration as Schmidt et al. [13], which is a cone model with a cylindrical injector section. Particular focus is given to the stability characteristics of the injection layer and whether these properties are more similar to those of a “conventional” boundary layer, as has been assumed in many previous studies, or a shear layer.

II. Experimental Setup

All experiments were performed in the Mach 4 Ludwieg tube at Caltech. The wind tunnel produces Mach 4 flow of nitrogen with a free stream velocity of 670 m/s, a steady test time of 60 ms, and a unit Reynolds number (\hat{Re}) in the range of $5\text{--}25 \times 10^6$ per meter. The noise level is approximately 0.7% in pitot stagnation pressure. Experiments were performed at \hat{Re}_∞ of 9 and 18×10^6 per meter, corresponding to free stream pressures of 1.2 and 2.4 kPa, respectively. The Ludwieg tube is operated with a fast-acting valve that seals near the nozzle throat and is removed rapidly to start the flow. The valve is described in detail in Sec. 2.2 of Schmidt [15].

Experimental data were acquired for varying injection mass flow rates for each of the injected gases listed in Sec. II.B at $\hat{Re} = 9 \times 10^6$ per meter and 18×10^6 per meter. Note that the unit Reynolds number in the test section of the Ludwieg tube depends only on the density in the free stream, because the reservoir gas is always at room temperature. Consequently, Reynolds number, free stream pressure, and density cannot be varied independently.

The test article consists of a 131-mm-long, sharp-tipped aluminum cone section with a measured tip radius of $300 \mu\text{m}$, followed by a 40-mm-long injector section, followed by a frustum. The cone has a half-angle of 5° , and the frustum is instrumented with five PCB 132A31 piezoelectric pressure transducers along its length at locations indicated in Figs. 1 and 2. The injector section is made of sintered stainless steel and is manufactured by Mott Corporation. The injected gas is pumped through the rear of the cone to the interior of the injector section; see Schmidt et al. [13].

A. Imaging System

Schlieren imaging is used as the primary diagnostic for this work. The framing rate of the imaging system must be sufficiently high to acquire converged statistics for the mean transition location of the

injection layer in a single wind tunnel run, and the exposure time must be short enough to freeze the motion of the transitional and turbulent structures in order to measure the transition location. These requirements lead to the use of a high-speed camera, here a Phantom v710 CMOS camera, and a pulsed laser diode light source; the system is nearly identical to the one described by Parziale et al. [16] except that the diode used in the current work is a stacked 3×3 array with a wavelength of 905 nm and a spectral bandwidth of 7 nm. The construction of the diode reduces both spatial and temporal coherence, and the emitter size is $200 \times 250 \mu\text{m}$. The reduced spatial coherence and large aperture eliminate the difficulties with using a traditional knife edge schlieren cutoff that are typically encountered with laser light sources. A similar technique has been applied to hypersonic boundary layers to measure second-mode instability waves [17–19].

Images of the entire test article were recorded in order to assess displacement due to injection. These were recorded at 30,262 frames per second at a resolution of 912×240 pixels with a scale of 0.18 mm/pixel. The pulse width of the light source is set to 40 ns. Higher-speed images for analyzing the stability of the flow are recorded at 289,361 frames per second with a resolution of 224×64 at the same scale as the full-field images. The pulse width of the laser diode is reduced to 25 ns to decrease motion blur and the duty factor in those cases.

B. Injected Gases

Pappas and Okuno [20] observed that the molar mass of the injected gas affects the transition location on a porous cone in Mach 4.8 flow. In the present work three gases with different molar masses were used in order to determine the effect of gas molar mass on the stability of the flow. Nitrogen is used as the reference gas with a molar mass matching the free stream gas, helium was used as the low-molar-mass gas, and the refrigerant RC-318 was used as the high-molar-mass (200 g/mol) gas. Some properties of the three gases used in the current work at 295 K are summarized in Table 1.

The mass flow rate of the injected gas is measured directly using a thermal mass flow meter, which was calibrated using a precision rotameter in series with the thermal meter. Flow through the injector is started several seconds before the wind tunnel is started to ensure that steady flow of the injected gas has been established and the flow meter gives an accurate reading. The meter has a rated accuracy of 1.5% of the full scale reading. The uncertainty used for error

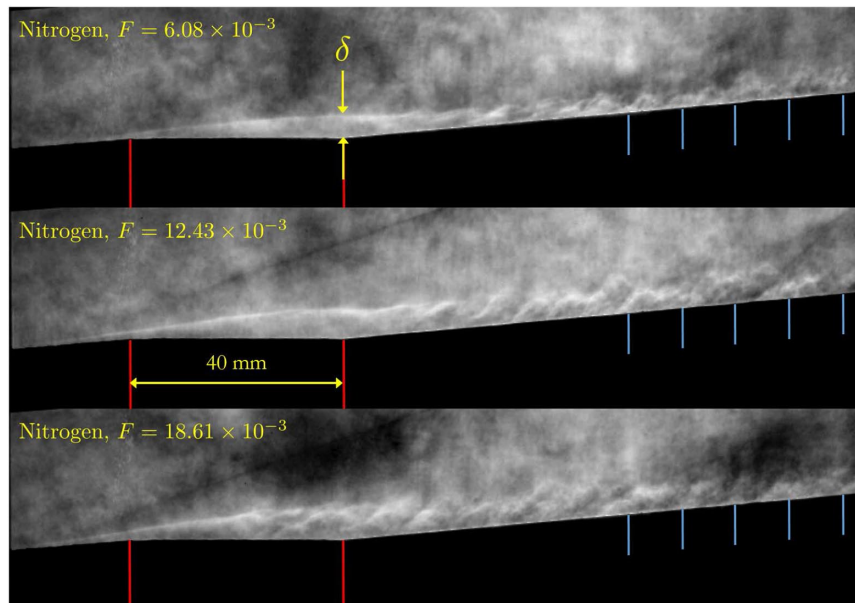


Fig. 1 Schlieren images with a 40-ns-pulse width from three cases with nitrogen injection at different injection rates. The injector is marked by red lines, and the locations of PCB pressure transducers are shown with blue lines. F can be converted to a normalization using the local conditions over the cone by multiplying by 0.85 [see Eq. (2)].

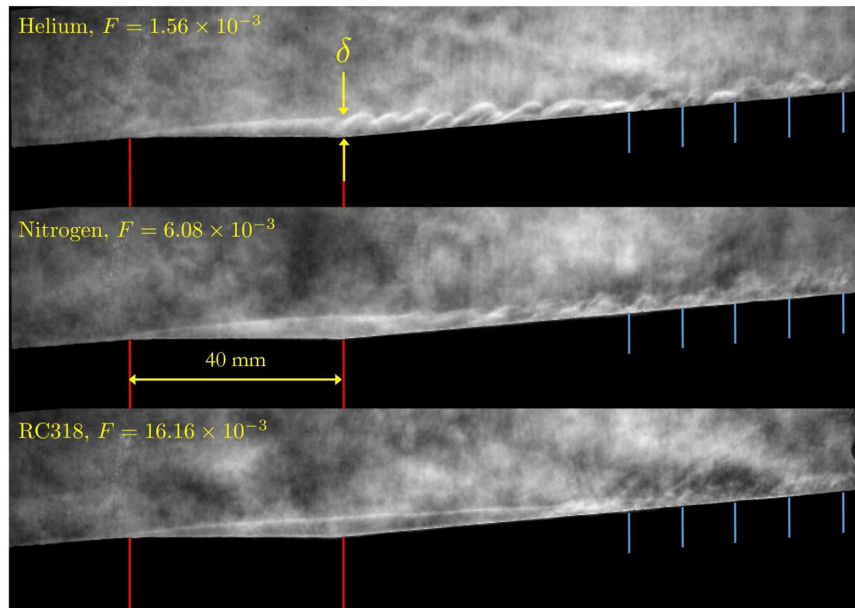


Fig. 2 Schlieren images with a 40-ns-pulse width from three cases with different injected gases but the same value of δ . The injector is marked by red lines, and the locations of PCB pressure transducers are shown with blue lines.

propagation is twice this value to conservatively account for potential errors incurred by the calibration process.

C. Computations

The experiments performed in this work were complemented by unsteady simulations of the Navier–Stokes equations using the open-source finite-volume CFD package OpenFOAM [21]. The specific flow solver used is a modification by Arisman et al. [22] of the well-known rhoCentralFoam solver (rhoCentralBinaryFoam) and includes diffusion of species assuming Fickian diffusion and realistic mass diffusivities for each species. rhoCentralBinaryFoam uses a finite volume discretization to solve the continuity, momentum, energy, and species diffusion equations with the second-order, semi-discrete, nonstaggered central-upwind scheme of Kurganov and Tadmor. Time derivatives are discretized using an implicit Euler scheme [23]. The simulation is laminar and unsteady. Steady-state solutions are found by marching forward in time until the mean flow has converged.

The simulations use a 2-D axisymmetric grid that extends from 10 mm ahead of the cone tip to 70 mm downstream of the end of the injector section. A quasi-steady state solution is first computed on a coarse grid, then the result is mapped to a grid that is highly refined near the wall, and the solution is again marched forward in time until a new quasi-steady state is reached. Waves appear in the injection layer downstream of the injector so that the flow is never truly steady for the entire field but the flow ahead of the injector does become steady after a sufficient number of time steps. A study was performed to ensure sufficient spatial resolution for grid independence; the final refined grid has a total of 755,857 points with a resolution of 45 μm per cell in the refined region, which gives a Reynolds number based on cell size of 405. For comparison, gradients in the injection layer occur over a region of approximately 3–10 mm depending on the case, corresponding to 70–220 cells through the interface region of the injection layer at the rear of the injector, which is the primary region of interest in this work. A grid independence study was performed for

a case with nitrogen injection at a tuned injection rate with eight grid resolutions from 38 to 191 $\mu\text{m}/\text{cell}$, which indicated that the high-gradient region in the injection layer was well-resolved for grid resolutions finer than 69 $\mu\text{m}/\text{cell}$ [15].

Boundary conditions are chosen to match the conditions in the Ludwig tube test section with a unit Reynolds number of 9×10^6 per meter. The velocity of the injected gas is prescribed as uniform across the injector surface, and a zero-gradient boundary condition is applied to the pressure. The temperature of the injected gas is fixed at 295 K. Solid walls are treated as adiabatic and a no-slip condition is applied to the velocity. Effects of wall temperature are very important for determining boundary-layer stability properties, but the computations in the present study are only used to compute the mean flow for scaling experimental results and not for performing stability calculations. Furthermore, the injected gas is at room temperature along the injector and along the wall immediately downstream of the injector where the instability waves are observed (see, e.g., Fig. 2), and therefore in this region the walls are very nearly adiabatic. An adiabatic wall assumption was found to be adequate for computing the mean flow for a similar flow configuration by Schmidt et al. [13]. An image showing the computational domain and a qualitative density field is presented in Fig. 3.

III. Results and Discussion

Figure 1 shows images for nitrogen injection at three flow rates. Flow over the same model configuration without injection is shown and described in [13], but will not be discussed in the present paper. In all cases, the near-wall flow created by injection is initially laminar near the injector, develops a shear-layer-like instability downstream, and ultimately transitions to a turbulent flow. The injector section is marked by vertical red lines in the images, and the locations of the PCB pressure transducers (used to record pressure fluctuations and analyze the flow instability) are marked by blue lines on the cone frustum. For these cases $Re = 9 \times 10^6$ per meter. The injection rates are reported in terms of F , the injected mass flux normalized by the mass flux of the free stream:

$$F = \frac{(\rho u)_{\text{inj}}}{(\rho u)_{\infty}} \quad (1)$$

The (visual) injection layer thickness δ is measured at the rear of the injector section for consistency. This choice is arbitrary because δ is observed to scale similarly with injection rate at any fixed location

Table 1 Properties of injected gases at 295 K

Gas	Symbol	Molar mass (W), g/mol	Specific heat ratio (γ)	Sound speed, m/s
Helium	He	4.00	1.67	1011
Nitrogen	N ₂	28.02	1.4	350
RC318	C ₄ F ₈	200.04	1.054	114

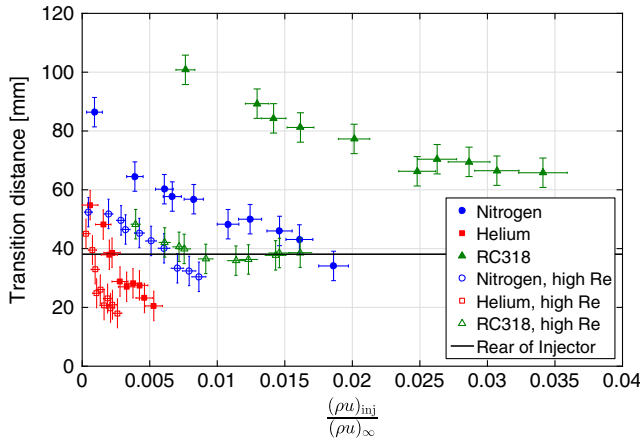


Fig. 3 Transition location determined from schlieren images for all experimental cases, relative to the front of the injector section, plotted against nondimensional injection mass flux F . The rear of the injector is marked as a horizontal line in the figure.

near the injector. The trends are that δ increases and the transition location moves upstream with increasing injection rate.

Figure 2 shows a set of images but for cases with different injected gases at the same value of Re (9×10^6 per meter) as Fig. 1. The injection rates in these cases were chosen such that δ is approximately the same for all three, and each one represents a tuned case. We observe that a lighter injected gas causes the transition location to move upstream. Both of the observed trends for transition location agree qualitatively with the findings of Pappas and Okuno [20] and Schmidt et al. [13], who examined the case of CO_2 and air injection with the same model as used in this study. Additionally, the flow downstream of injection in the schlieren images in Figs. 1 and 2 is qualitatively similar to that shown in the shadowgraph images of Pappas and Okuno [20]. The trends are shown for all cases as a function of injection mass flow rate F in Fig. 3. F is defined here using the free stream conditions as is typical in several other studies of flows with boundary-layer injection, but F can be instead defined using the local conditions over the cone computed with the Taylor-Maccoll solution for inviscid supersonic flow over a cone. F is defined this way by Pappas and Okuno [20]. The free stream and local conditions are related by

$$\frac{\rho_\infty u_\infty}{\rho_l u_l} = 0.85 \quad (2)$$

It is noted from Fig. 3 that the injection flow rates in this study overlap with those of Pappas and Okuno [20] and include higher flow rates as well, unlike a previous study on the same model geometry, which only included higher flow rates [13].

The instability waves in the three cases also appear to have a different character depending on the injected gas. With helium injection the waves appear as large-amplitude “rolling” structures reminiscent of those observed in free shear layers (e.g., by Brown and Roshko [24]). The waves in the nitrogen injection cases are lower in amplitude and more sharply inclined by comparison. Waves in RC318 injection cases are quite different from those present in cases with the other injected gases. They are difficult to visualize in single images because they have a very long wavelength, but slow oscillations in the interface are visible when a sequence of images is viewed as a movie. It is argued in Sec. III.B.2 that this difference in behavior is due to a supersonic convective Mach number of the instability waves and the proximity of the cone wall, resulting in a different most-unstable mode leading to transition.

Figure 3 shows the observed mean transition location as a function of injection flow rate for cases with all three injected gases. The transition location is reported in dimensional units measured in reference to the front of the injector section so that the transition front can be compared with the model geometry. Solid symbols have a nominal unit Reynolds number of 9×10^6 per meter, while hollow

symbols (labeled as “high Re” in the figure) have a nominal unit Reynolds number of 18×10^6 per meter. This labeling scheme is used throughout the paper. The transition location is determined by noting where the interface between the injected and free stream gases ceases to be smooth and laminar. This method is less reliable than data from thermocouples or pressure transducers, but is sufficient for determining trends in the data.

Comparing Figs. 1 and 2 indicates that the conditions that result in a tuned case, that is, when the edge of the injection layer is tangent to the cone wall at the start of the injector section, do not depend only on F , but the tuned condition does appear to correspond to a unique value of the displacement thickness δ . This indicates that F is not the appropriate nondimensional parameter for correlating the results. A parameter based on the flow rate that can predict a value of δ for any injected gas is therefore presented in Sec. III.A.

Figures 1 and 2 also demonstrate the quality of the images acquired with the pulsed laser diode light source. The images in the two figures have been minimally postprocessed, with only some contrast enhancement and partial background subtraction to improve clarity. The effective incoherence of the light source gives nearly speckle-free images, although there is some nonuniformity in the illumination across the image and between multiple images from the same experiment.

A. Injection Layer Thickness

The nondimensional momentum flux J is determined to be a better parameter for prescribing the injection rate than F by considering the injection process as a low-momentum jet in a supersonic crossflow. The review by Mahesh [25] summarizes the work of several researchers who find that the jet trajectory, which is related to the penetration height, is primarily a function of the momentum flux ratio J :

$$J = \frac{\rho_j u_j^2}{\rho_\infty u_\infty^2} \quad (3)$$

Similarly to F , one can alternatively define J based on the local conditions over the cone rather than the free stream conditions. The free stream momentum flux is related to the momentum flux over the cone by

$$\frac{\rho_\infty u_\infty^2}{\rho_l u_l^2} = 0.86 \quad (4)$$

The trajectory will also depend on the density and temperature ratios of the jet to the free stream as well as the molar masses and Mach and Reynolds numbers of the jet and free stream. Most empirical correlations neglect these dependencies, however, and take the form

$$\frac{y}{d} = \text{fn}\left(J, \frac{x}{d}\right) \quad (5)$$

The functional dependence on J and x/d is often cast as a power law, with different exponents on J and x/d .

Under these assumptions, at a fixed location x the penetration height y can be considered a function of J only. In the present work, y/d at the rear of the injector is analogous to δ/L_{inj} , where L_{inj} is again the length of the injector section. The momentum flux of the injected gas is computed by assuming that the average pressure over the injector is the same for all experiments, which allows the density to be extracted from the measured mass flux. The pressure is determined by averaging the pressure at the injector exit in the OpenFOAM computations.

The measured visual injection layer thickness δ is plotted versus J in Fig. 4 along with the results from the OpenFOAM computations, using the maximum gradient in the index of refraction to determine the visual thickness. δ is nondimensionalized by the length of the injector L_{inj} , but this choice is arbitrary because the model is identical for all cases. The vertical error bars represent the uncertainty in δ due

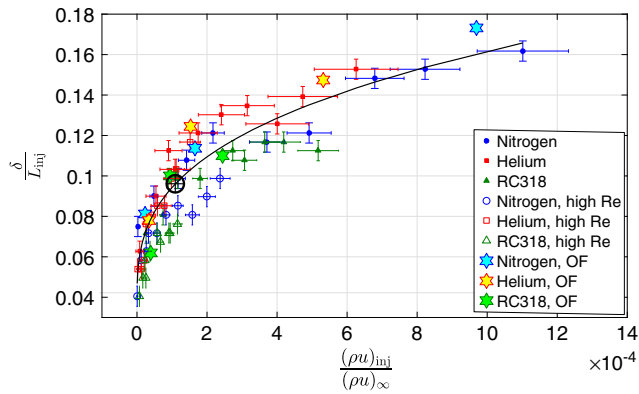


Fig. 4 Injection layer thickness measured at the rear of the injector section, normalized by the injector length, plotted versus the nondimensional momentum flux J . High-Reynolds-number cases have $Re = 18 \times 10^6$ per meter. The \oplus symbol indicates the tuned condition. Here and in the figures that follow in this work, J can be alternatively defined by the local conditions over the cone by multiplying by 0.86 [see Eq. (4)].

to the finite resolution in the images. Horizontal error bars are calculated from both the uncertainty in measured injection mass flow rate and the uncertainty in free stream conditions (assumed to be $\pm 5\%$ for all variables) using standard error propagation. The black curve in the figure is a power law fit to the data with a calculated fit of

$$\frac{\delta}{L_{inj}} = 1.256 J^{0.333} + 0.0358 \quad (6)$$

Mahesh's review article [25] reports values between 0.276 and 0.5 for the exponent on J . Defining J based on local conditions over the cone does not change the value of the fitted exponent 0.333.

B. Injection Layer Stability

1. Data Processing

Images acquired to investigate the instability in the injection layer are processed using background subtraction and contrast enhancement before analysis. A description of the processing routine is given in Sec. 4.2 of [15]. A series of 10,000 images taken at 289,361 frames per second is acquired for each wind tunnel run.

The wavelength of the instability waves is determined by performing an autocorrelation of the portion of each image containing visible waves. The accuracy of autocorrelation in this case is limited by the digitization of the images, and so the uncertainty in each measurement is approximately $200 \mu\text{m}$. Figure 5 shows a sample image from an experiment with nitrogen injection to show the measurement location relative to the model. The smaller inset image in Fig. 5 is taken at the higher frame rate of approximately 290 kHz listed in Sec. II.A, whereas the larger full-field image is taken at the lower frame rate of 30 kHz. The dashed yellow lines show the region of the image that is used for autocorrelation; it is centered on the

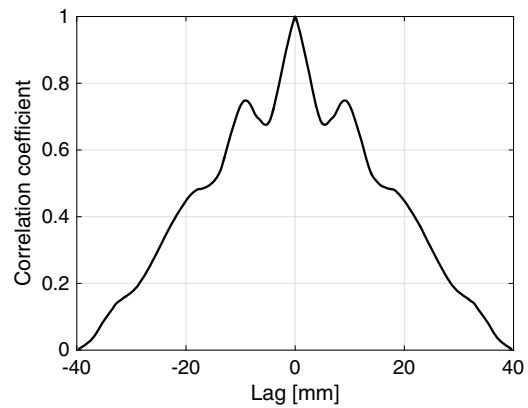


Fig. 6 Autocorrelation for the image shown in Fig. 5. The secondary peak at nonzero lag corresponds to a wavelength of 9 mm.

interface between gases. The correlated region is translated horizontally to produce the autocorrelation curve.

The autocorrelation associated with Fig. 5 is shown in Fig. 6. The feature of interest is the secondary peak at a lag of approximately 9 mm, which corresponds to the wavelength observed in this image. Not every image produces an autocorrelation with such a pronounced secondary peak, due to both intermittent turbulent bursts in the flow and the unsteady nature of any transition process. To use this peak to define the instability wavelength, we place constraints on the absolute value of the peak at nonzero lag, its relative magnitude relative to the magnitude of the curve at the local minimum between the peak at nonzero lag and the maximum at zero lag, and the slope of the curve between the local minimum and the peak at nonzero lag. These constraints were used to set cutoff values for accepting data sets; the values were determined by examining individual images where a dominant wavelength was clearly apparent and those where no wavelength appeared and adjusting the values until data sets with well-defined instability waves were being accepted. Changing the cutoff values by small amounts does not change the result of the algorithm significantly. For a given case with 10,000 images, 2000–4000 images will typically contain a wavelength that meets the criteria.

The distribution of wavelengths for a given wind tunnel run is fitted with a log-normal distribution to eliminate difficulties associated with negative population values associated with using a Gaussian distribution to approximate a data set, and the maximum of the distribution is used to represent the wavelength for a single experiment. In cases with RC318 injection, the wavelengths are too long to determine by autocorrelation, and so they are computed from their measured convective speed and frequency: $U_c = \lambda f$. The wavelength normalized by the length of the injector is plotted versus J in Fig. 7. Here and throughout this work, vertical error bars represent the standard deviation of the underlying distribution for each case, not the measurement uncertainty, indicative of the level of natural variations present in the transition process in this flow. This is an important distinction that should be kept in mind when interpreting the presented results. The standard deviations of the means of the plotted data are much smaller by comparison, on the

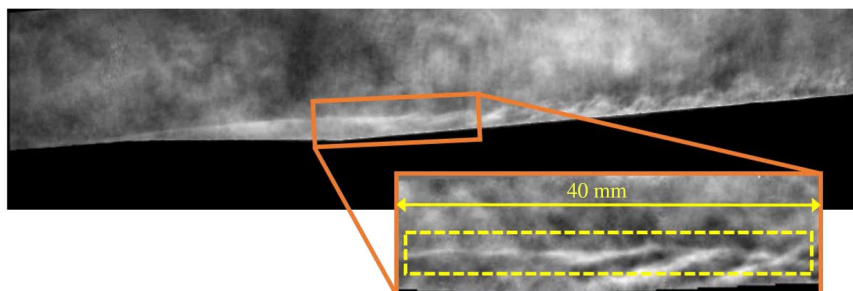


Fig. 5 Processed image (inset) showing instability waves to be analyzed by autocorrelation, from a sequence taken at 290 kHz. The full field image is included to show the location for 290 kHz imaging relative to the 30 kHz imaging. The yellow dashed lines show the region used for autocorrelation.

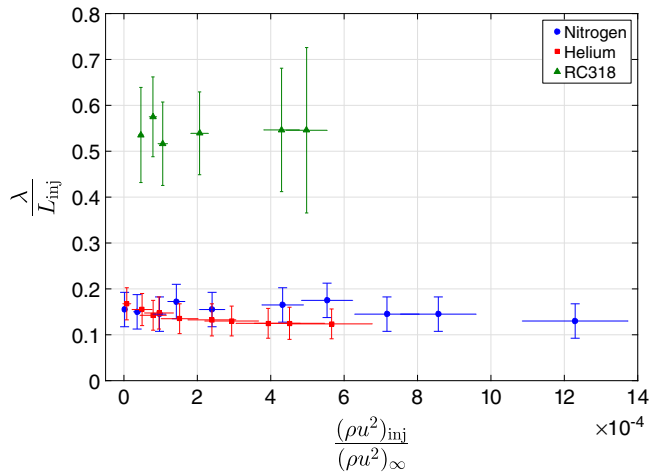


Fig. 7 Wavelength normalized by the injector length plotted against the nondimensional injection rate J for all cases analyzed. The wavelength is measured directly for helium and nitrogen injection and calculated using convective speed and frequency for RC318 injection.

order of the size of the data points in the figures. The wavelength is nearly independent of injection rate for a given gas, although the injection layer thickness δ varies by a factor of three. This is contrary to the behavior of instability waves in boundary layers, whose wavelengths scale with the local boundary-layer thickness.

The convective speed of the instability waves can be determined relatively easily by image cross-correlation. The same region used to detect the wavelength is used for cross-correlation. In nitrogen and helium injection cases, only images with waves present are correlated with their neighbors to avoid incorrectly tracking other phenomena, such as turbulent bursts. Images are correlated with each of the four previous images in an attempt to mitigate pixel locking. In cases with RC318 injection cross-correlation is attempted near the interface of the gases for all images, and so the results in those cases are less accurate than those for nitrogen and helium injection.

Figure 8 shows a sequence of images from a case with nitrogen injection. The frame rate is sufficiently high that the waves move only a few millimeters between images. Motion of the waves is indicated by the arrow in the figure.

As with wavelength detection, a criterion is applied to a correlation curve to determine if a velocity can be reliably measured. To be accepted for velocity measurement, the peak of the curve must occur at a nonzero lag and must have an absolute value greater than a specified cutoff. The data are again insensitive to the cutoff value; one is chosen to obtain 1000–2000 velocity measurements in most cases. The lag is converted to a velocity by multiplying by the framing rate, assuming a constant velocity between frames.

A population of velocity measurements is produced for each tunnel run. The mean and standard deviation of the population are used to calculate a single value and uncertainty for a given case. Figure 9 shows measured convective velocities for all cases. Error bars for the RC318 cases are quite large, reflecting the reduced accuracy in those measurements because images with waves could not be as reliably identified as in the nitrogen and helium cases. The data show no discernible trend for nitrogen injection with increasing injection mass flow rate, whereas for helium injection an increase in convective velocity with increasing injection rate is observed and for RC318 injection it appears that the velocity may be decreasing with increasing injection rate.

The frequency of the waves is determined from imaging from the convective speed and wavelength for nitrogen and helium injection cases, using a strategy similar to that employed by Kennedy et al. [19]. With RC318 injection, however, it can be measured directly in most cases. The edge of the injection layer in these cases is reasonably stable in time and easy to see with the naked eye, and so the Prewitt edge-detection routine is used to find a point along the edge and track it from image to image. Its position moves up and down as waves pass, and the frequency can be extracted by temporal Fourier

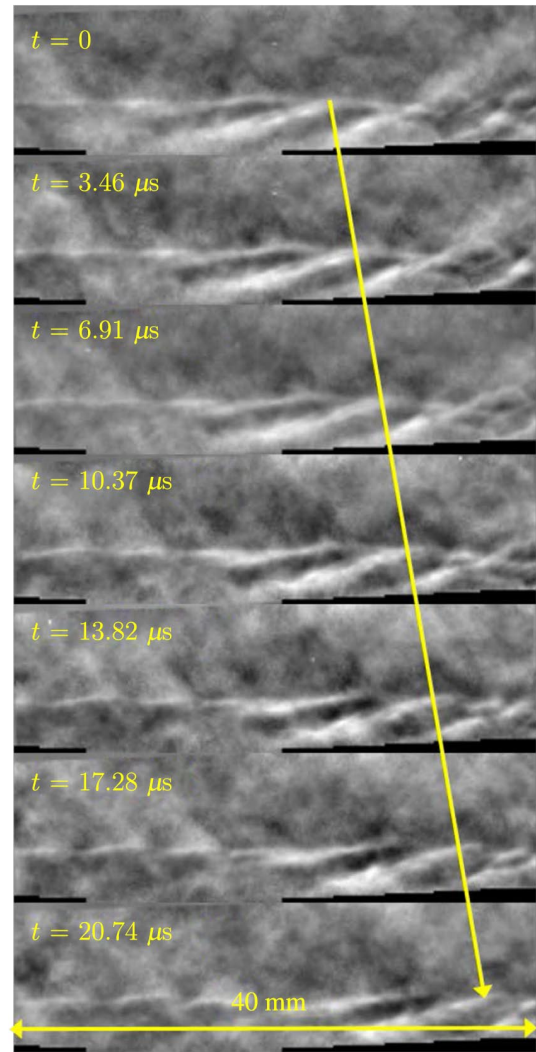


Fig. 8 Series of images of a case with nitrogen injection showing the propagation of waves. Their velocity is determined by cross-correlating the region in the images where the waves are present.

analysis. Figure 10 shows a power spectral density spectrum for the example case; it exhibits a peak at 24.5 kHz.

Data from the PCB pressure transducers were also analyzed for each case. Temporal Fourier analysis was applied to detect frequencies. Many cases, particularly for nitrogen injection, do not

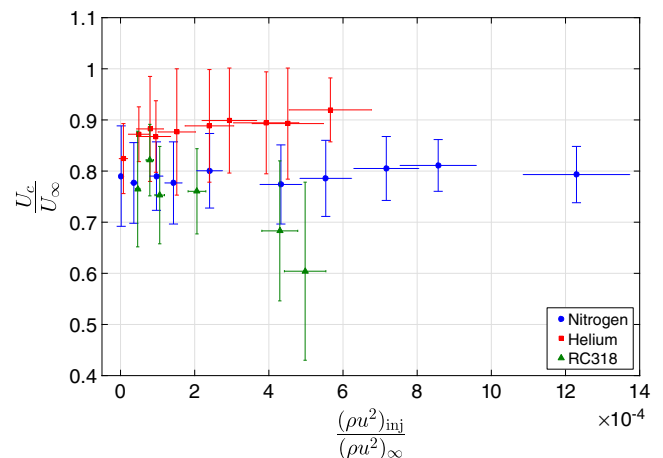


Fig. 9 Convective velocity normalized by the free stream velocity plotted versus the nondimensional momentum flux J for all cases studied. Vertical error bars represent the standard deviation in the population of measured velocity values.

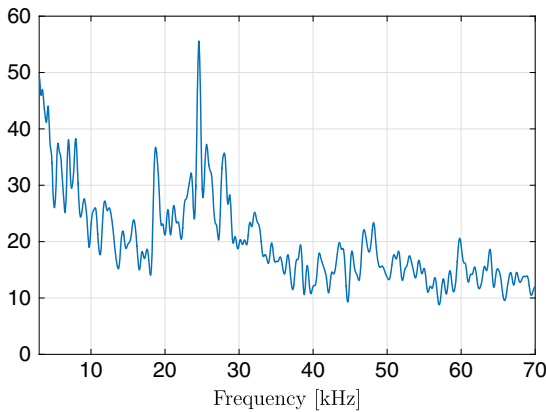


Fig. 10 Power spectral density from the edge-finding routine for the example RC318 injection case. A peak is observed at 24.5 kHz.

show a significant peak in the spectra for any of the transducers. This could have several causes. First, the instability waves are not consistently present in the flow field due to the intermittent nature of the transition process, and in order to be detected by the pressure transducers they need to not only be present but also occur very near to the transducers. This could prevent the transducers from detecting a single frequency. Second, the pressure fluctuations from the instability waves may be somewhat localized to the interface between the injected gas and free stream gas and do not propagate to the wall of the model consistently. Finally, the transducers may be located too far behind the onset of transition to measure the frequency of the waves before they break down to turbulence. The location of the transducers relative to the transition location can be seen for a few cases in Fig. 2. Figure 11 shows the spectrum from one transducer for one such case with helium injection. The spectrum is compared with the spectrum from the same transducer for a flow with the same injection rate, but with a boundary-layer trip upstream of the injector to make the injection layer fully turbulent. A clear peak at 101 kHz is observed in the laminar spectrum.

Frequency data from image analysis and, when it can be obtained, from the pressure transducers are plotted together in Fig. 12. The frequencies are normalized by the length of the injector and the free stream velocity to form a Strouhal number. The uncertainties in the nitrogen and helium visualization data are estimated by propagating the uncertainties of the wavelength and velocity data. Uncertainty in frequency for the RC318 visualization data and all pressure transducer data is calculated from the full width at half maximum of the peak in the spectra. The frequency is relatively constant for nitrogen injection cases, increases with increasing injection mass flow rate for helium injection cases, and decreases slightly with

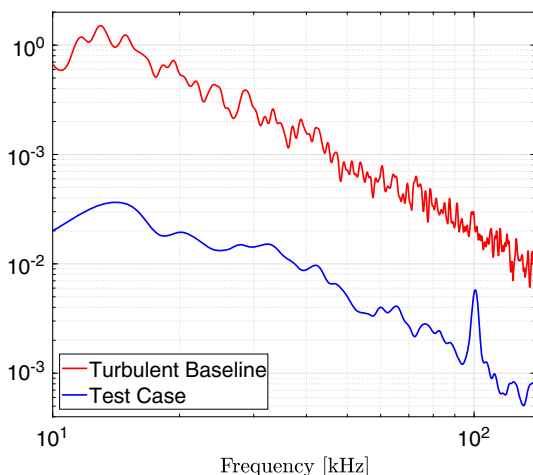


Fig. 11 Spectra for a case with helium injection and a case with the same injection rate but a fully turbulent injection layer caused by a boundary-layer trip upstream of injection.

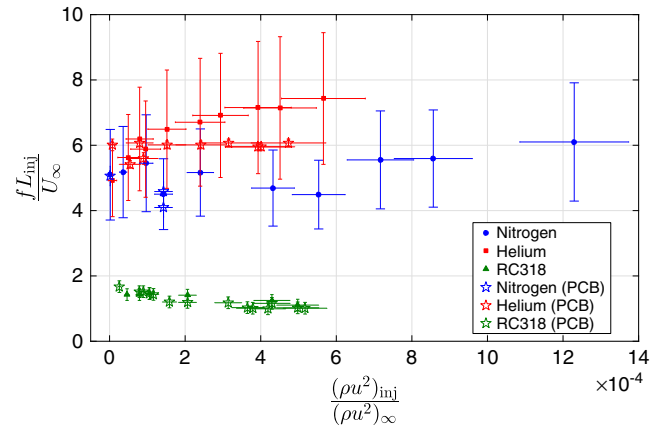


Fig. 12 Frequency from image analysis and pressure transducers. The frequency from image analysis for the helium and nitrogen injection cases is computed from the measured convective speed and wavelength, whereas the frequency in the RC318 cases is computed directly from the image processing routine.

increasing injection mass flow rate for RC318 injection cases. The trend for the PCB data for helium injection cases is that the frequency is approximately constant for high injection rates instead of increasing as in the imaging data, but the imaging data are considered to be more reliable in this study because of the difficulties outlined above in extracting reliable data from the PCB sensors. Nevertheless, the two methods agree within experimentally observed variations in the imaging data.

Regarding the computations described in Sec. II.C, data are primarily analyzed in terms of wall-normal profiles of flow variables. Locations are marked by orange arrows in Fig. 13. One profile is taken of the incoming boundary layer near the end of the cone tip section, three profiles are taken over the injector, and four are taken on the frustum section downstream of the injector section. The distances measured along the cone surface from the tip of the cone for each profile are 120, 132.5, 152, 172, 180.6, 189.2, 197.8, and 206.4 mm, respectively.

2. Instability Analysis

Fedorov et al. [26] and Schmidt et al. [13] performed theoretical studies on the stability of flow with injection on the geometry used in the current work using linear stability analysis. Both studies were performed with air injection into an air free stream, and so do not include effects of varying the injected gas. Both studies found that injection destabilizes several acoustic modes, but the mode with the highest growth rate is two-dimensional. The most amplified frequency, nondimensionalized using the length of the injector and free stream velocity as in Fig. 12, is found by Schmidt et al. [13] to be approximately 5.2, which agrees with the frequency found for nitrogen injection in this work. Neither of these theoretical studies investigates the waves in the nonlinear regime, but the waves observed in this work by schlieren visualization are likely nonlinear.

As mentioned in Sec. III.B.1 in reference to Fig. 7, the wavelength and other measured properties do not scale directly with the injection layer thickness, which is not the case for the instabilities dominant in

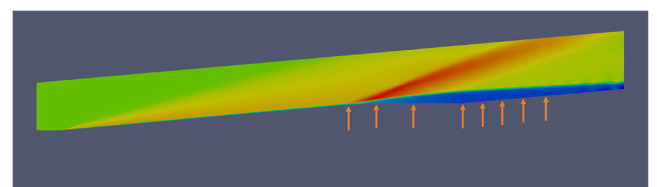


Fig. 13 Location of wall-normal profiles for all OpenFOAM cases. They are located 120, 132.5, 152, 172, 180.6, 189.2, 197.8, and 206.4 mm from the cone tip, measured along the surface of the model. A case with nitrogen injection is shown as an example. The domain is colored according to density.

supersonic boundary layers [27]. This indicates that transition in supersonic flow with injection is due to another mechanism. Flow with injection involves the mixing of two streams of different velocities, which suggests that its stability characteristics may be similar to those of shear layers.

Two-dimensional free shear layers are a canonical flow in fluid mechanics. Information about the stability of free shear layers can be found in the literature [28–33], and in the review paper by Dimotakis [34]. A quantity called the vorticity thickness is the most common length scale used to nondimensionalize features in both compressible and incompressible shear layers.

$$\delta_\omega = \frac{U_1 - U_2}{(du/dy)_{\max}} \quad (7)$$

Stream 1 is defined to be the higher-speed stream in the shear layer. Another important quantity for shear layers is the convective Mach number, defined for stream j as

$$M_{c_j} = \frac{U_j - U_c}{a_j} \quad (8)$$

Shear layers are generally more stable with increasing convective Mach number. The convective speed U_c of structures in a compressible shear layer is shown by Papamoschou and Roshko [29] to be predicted by the conditions in the two streams, after substitution of Eq. (8).

$$\left(1 + \frac{\gamma_1 - 1}{2} M_{c_1}^2\right)^{\gamma_1/(\gamma_1 - 1)} = \left(1 + \frac{\gamma_2 - 1}{2} M_{c_2}^2\right)^{\gamma_2/(\gamma_2 - 1)} \quad (9)$$

Equation (7) cannot be applied directly to the velocity profiles because although there is a clear choice for the parameters for stream 1 (the free stream values over the cone), there is not a clear choice for stream 2 conditions because of the influence of the wall. The profiles produced by the OpenFOAM computations can be used to calculate an equivalent length scale to nondimensionalize the wavelengths observed in experiments. This can be resolved by defining a new thickness δ_c , which is the vertical distance between the points of maximum curvature of the momentum profile. δ_c will be referred to in this work as the curvature thickness of the profile. It is roughly equivalent to δ_ω except that it allows for either or both of conditions 1 and 2 to be not well-defined. It is only required that there is an inflection region in the profile. The momentum profile is chosen instead of the velocity profile, motivated by the fact that many features in jets, wakes, and shear layers depend on the initial momentum thickness [33]. The velocity and momentum profiles yield very similar results in most cases, with slight differences because the density and velocity profiles evolve differently due to the presence of the wall and convection of the injected gas in the direction normal to the mean flow from the injector. This is not a concern in free shear layers where the velocity and density profiles behave similarly to one another. An example momentum profile for a case with nitrogen injection is shown in Fig. 14 with the curvature thickness indicated.

δ_c increases with downstream distance as streamwise momentum diffuses downward from the free stream toward the wall, and so a common choice of streamwise location between all cases at which δ_c is evaluated is necessary. Figures 1 and 2 indicate little variation in wavelength of the instability waves with downstream distance for a given injected gas and flow rate. It is therefore assumed that the instability begins at the beginning of the injector when the interface between the free stream and injected gases is displaced from the wall. This observation of the lack of variation in wavelength with downstream distance may be related to the well-known effect of the wake of the splitter plate on planar shear layer growth [35]. Hence the momentum profiles at the front of the injector are used to evaluate δ_c for each case. There is some difficulty in locating the furthest point of curvature from the wall in cases where a strong shock is present at the beginning of the injector section, and so the uncertainty in δ_c is higher

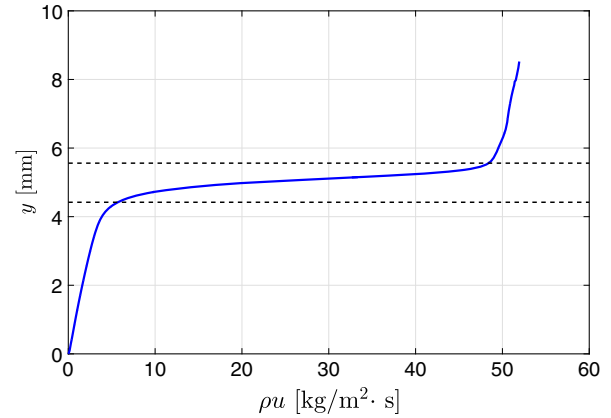


Fig. 14 Example momentum profile for a case with nitrogen injection. The curvature thickness δ_c is indicated with black dashed lines.

in these cases. Figure 15 shows the experimental values for wavelength normalized by corresponding values for δ_c from the computations.

The results for nitrogen and helium injection collapse to a value of $(\lambda/\delta_c) = 8.5$, and the results for RC318 injection are self-consistent in the sense that the measured wavelength and calculated δ_c are both approximately constant across all injection rates tested. The value of 8.5 is higher than the values reported in the literature for (λ/δ_ω) of between 3 and 5 for free shear layers [24,28,30], but there is a difference between the definitions δ_c and δ_ω used to normalize the wavelength, and so some discrepancy is expected. It is not possible to define a value for δ_ω in the present study because of the difficulty of determining appropriate values of U_1 and U_2 described above, but it is clear from Fig. 14 that for a free shear layer, δ_ω would be larger than δ_c , so values of (λ/δ_ω) would be smaller than corresponding values of (λ/δ_c) . For example, a hyperbolic tangent function (\tanh) is commonly used to approximate shear layer velocity profiles. δ_ω for $\tanh x$ is 2, whereas $\delta_c = \text{arccosh}(2) \approx 1.32$.

The values of (λ/δ_c) for RC318 injection cases are much higher than those for helium and nitrogen injection, however. This may be because the momentum profile for RC318 injection has an additional inflection region close to the wall where the density reaches a local maximum, which is not present in the velocity profile. This could change the scaling of the wavelength relative to the other cases where the momentum profile is monotonic. The fact that the curvature thickness collapses the wavelengths in each data set in this study much in the same way that the vorticity thickness collapses the wavelength data in free shear layers is evidence that the instability present in supersonic flow with injection may be of the same type as that active in supersonic shear layers.

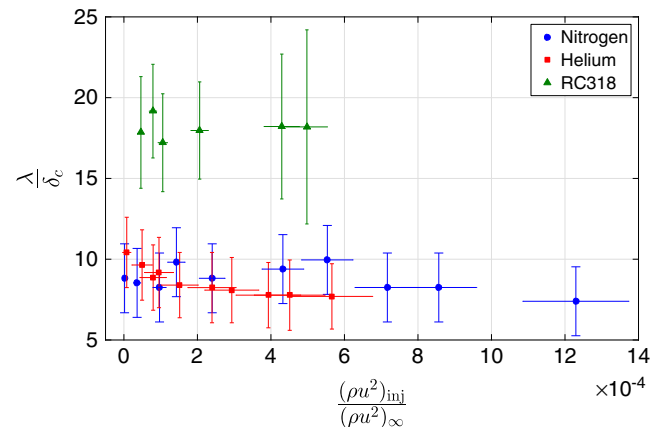


Fig. 15 Wavelength normalized by δ_c using the values determined from the computations for each corresponding case. Values of δ_c are interpolated over the various values of J for cases with each injected gas.

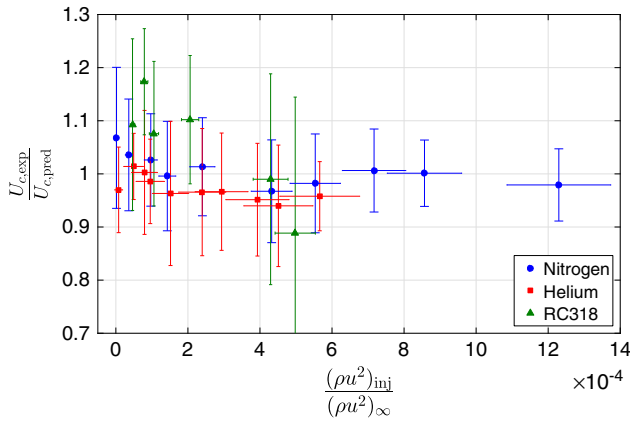


Fig. 16 Ratio of the measured experimental value of wave convective speed to that predicted using Eq. (9) and the computations plotted against J for cases with a nominal unit Reynolds number of 9×10^6 per meter.

Predicting a convective velocity for waves in the injection layer is not straightforward using Eq. (9) and the data from the OpenFOAM computations. Condition 1 is obviously the free stream over the cone, but the choice of condition 2 is not clear because of the presence of the wall. Based on a similar argument to the one used to define δ_c , namely, that the properties of the layer are governed by the inflection region in the momentum profile as long as the inflection point is sufficiently far from the wall, condition 2 can be specified at the lower point of curvature in the momentum profile, which is indicated by the lower dashed line in Fig. 14. Using this definition for condition 2, the value of U_c calculated from Eq. (9) varies only slightly in the streamwise direction. The profile used to compute U_c is the one at the rear of the injector, which is close to where the convective speed is measured in the experiments. The inflection point in the momentum profile is several δ_c s from the wall at this location. Figure 16 shows the measured convective velocity for each experiment normalized by a corresponding predicted convective velocity from Eq. (9) and the OpenFOAM data.

Using the lower point of curvature in the momentum profile to calculate the conditions in stream 2 for Eq. (9) predicts the measured convective velocity closely for all cases. Recall from Sec. III.B.1 that there is some additional uncertainty in computing the convective velocity in cases with RC318 injection because the long-wavelength structures are difficult to track with the limited camera resolution available. The fact that the convective velocity of structures in the injection layer can be so accurately predicted using a relation for free shear layers, along with the evidence provided by the scaling of the wavelengths, provides a strong case that the instability present in the injection layer is of the Kelvin-Helmholtz type resulting from the inflection in the velocity profile.

If transition in flow with injection is due to shear layer instabilities, then the findings of past research efforts on shear layers can be brought to bear on understanding and predicting the behavior of flow with injection under different conditions, beyond just predicting the wavelength, velocity, and frequency of the waves. First, Brown and Roshko [24] report that the vorticity thickness is lower for shear layers with a heavier gas in the high-speed stream, or, equivalently, for a lighter gas in the low-speed stream. The same qualitative trend is observed in the current work. Inspection of Fig. 7 shows that the λ , and therefore δ_c , for the injection layer is indeed thinner for lighter injected gases, which constitute the majority of the low-speed stream.

Since its introduction, many researchers (e.g., Papamoschou and Roshko [29]) have noted the importance of the convective Mach number in representing the effect of compressibility on a shear layer. M_c is particularly important in predicting the amplification rate of disturbances in a compressible shear layer and therefore its stability. As noted by Papamoschou [28], M_c is a function of y , the coordinate normal to the mean flow direction, in shear layers with finite thickness. M_c is plotted as a function of y at the rear of the injector section for three example cases, one for each injected gas, in Fig. 17. The profiles of $M_c(y)$ are very similar for cases at injection rates other than the ones shown in the figure. Black dashed lines mark the location of the points of maximum curvature in each case's momentum profile, which are used to specify the conditions of streams 1 and 2.

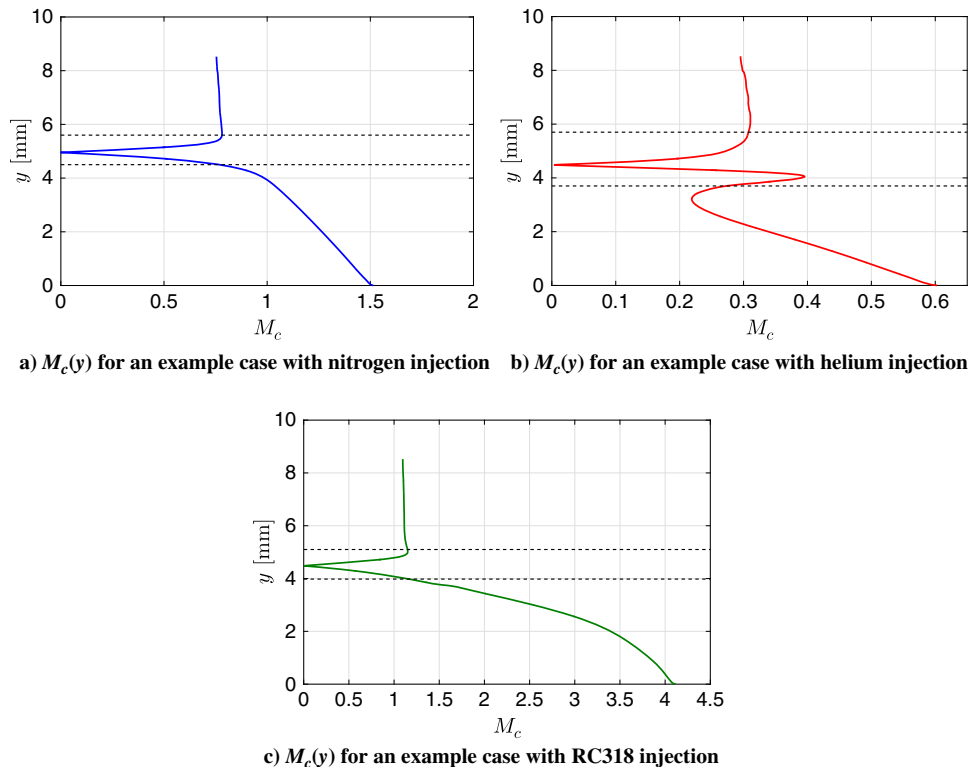


Fig. 17 Convective Mach number M_c plotted as a function of the wall-normal coordinate y for three example cases. Profiles are taken at the rear of the injector section. The black dashed lines in each plot mark the location of the curvature points in the corresponding momentum profile.

The convective Mach number increases close to the wall and becomes supersonic in cases with nitrogen and RC318 injection. This is a feature that is not observed in free shear layers, and so it is unknown how this affects the transition process. It should also be noted that a subsonic sublayer exists in the center of the inflection region of the momentum profile where the convective Mach number is small in all cases, a feature also observed by Papamoschou and Roshko [29] for free shear layers.

It has been well-documented that the amplification of disturbances in a shear layer decreases with increasing M_c , and therefore shear layers with higher convective Mach numbers are more stable. This explains the trend in transition location observed in the experiments performed in this study and also past studies that have observed the same trend; that is, the transition location moves downstream as the molar mass of the injected gas decreases [13,20,36]. Figure 17 shows that the convective Mach number increases with the molar mass of the injected gas, enhancing the stability of the resulting injection layer. Equation (9) indicates that the value of γ is also important in determining the convective velocity. This effect can be observed as $\gamma \rightarrow \infty$; in Fig. 17, where u and a approach common values for each case. Decreasing γ has the effect of decreasing the convective velocity of the instability waves, increasing the convective Mach number. γ is typically lower for gases with higher molar mass, and so these effects act together to increase M_c over the entire injection layer thickness.

M_{c1} and M_{c2} are subsonic in cases with nitrogen and helium injection and weakly supersonic in cases with RC318 injection. This difference may contribute to the different values observed in (λ/δ_c) (see Fig. 15). Papamoschou [28] observes a difference in (λ/δ_ω) in free shear layers when the convective Mach number changes from subsonic to supersonic, although in his work the wavelength becomes shorter as the convective Mach number becomes supersonic, which is the opposite of what is observed here. Sandham and Reynolds [37], Clemens and Mungal [38], and others have also documented that oblique modes can become active in compressible shear layers when the convective Mach number is sufficiently high, which could also help explain why the waves have different characteristics in cases with RC318 injection. The convective Mach number in nitrogen injection cases becomes supersonic close to the wall, but the instability behaves similarly to that in helium injection cases, and so it is possible that whether the convective Mach number is subsonic or supersonic is only important in between the points of maximum curvature where the shear is high.

The effect of the cone wall can be inferred qualitatively from the linear stability analysis of Zhuang et al. [39]. They consider a two-dimensional, constant-density, homogeneous shear layer propagating in a confined two-dimensional channel with frictionless walls on both sides of the shear layer. The analysis cannot predict the influence the profile shapes (density, temperature, etc.) of the injection layer have on the instability, but it does give some insight into how the walls interact with the shear layer. They find that for subsonic convective Mach numbers the walls have no discernible effect, but that the walls weakly destabilize the instability in cases with supersonic convective Mach number. Interestingly, they find that multiple instability modes are active in cases with supersonic convective Mach number and that the Kelvin-Helmholtz mode is not the most unstable mode. Disturbances are amplified by the reflection of acoustic waves generated in the shear layer from the walls. Both of these findings—there are multiple unstable modes when the convective Mach number is supersonic and the modes are amplified by acoustic wave reflection—are similar to the findings of Mack [27] for high-speed boundary layers. The cone wall likely has a similar influence on the injection layer in the current study.

The difference in behavior when the convective Mach number is supersonic in the presence of a wall or walls perhaps better explains the significant qualitative difference observed in the injection layer with RC318 as the injected gas compared with cases with the other two gases. If the most unstable mode is not of the Kelvin-Helmholtz type, then it may very well exhibit a different scaling for its wavelength from the other cases that are Kelvin-Helmholtz unstable. The most unstable mode in cases with RC318 injection may also be oblique. The mode of the instability would not affect the predicted

convective velocity, as the formulation of Eq. (9) for predicting the convective velocity does not require that the waves be of any particular type, so long as they exist between two streams with different speeds.

IV. Conclusions

Supersonic flow with injection has been studied with three injected gases with different molar masses in a configuration that is designed to compensate for the additional displacement to the boundary layer caused by injection in order to minimize the strength of waves in the flow. The nondimensional mass flux F has been used to characterize the injection rate in many previous studies, but the current work has shown that proper tuning depends on the injection layer thickness δ , which is not uniquely predicted by F when different injected gases are used. Considering the flow with injection as a weak jet in supersonic crossflow suggests the use of the nondimensional momentum flux J to predict δ , and the data collected in this work show that δ is well-described as a function of J only, even for injected gases with very different molar masses.

The wavelength, frequency, and convective speed of instability waves in the injection layer were measured using high-speed imaging. Along with data from numerical simulations, the instability is determined by scaling arguments, quantitative prediction and verification using computations and experiments, and qualitative trends in the data to behave like that dominant in supersonic shear layers rather than those in boundary layers. This finding differs from the instability modes considered in many previous studies of supersonic flow with injection, and calls for further experimental and numerical work.

Acknowledgments

The authors acknowledge funding from The Coco and Foster Stanback STEM Fellowship and the Air Force Office of Scientific Research under Grant No. FA9550-10-1-0491. The authors wish to thank Bahram Valiferdowski for assistance in the laboratory, and Joe Haggerty and Ali Kiani, as well as Mr. Valiferdowski, for assistance constructing the test articles. The authors thank Jason Schlup and Rich Kennedy for contributions to the development of the fast-acting valve for the Ludwig tube. Finally the authors thank Prof. Hans Hornung for helpful insights and guidance.

References

- [1] Aupoix, B., Mignosi, A., Viala, S., Bouvier, F., and Gaillard, R., "Experimental and Numerical Study of Supersonic Film Cooling," *AIAA Journal*, Vol. 36, No. 6, 1998, pp. 915–923. doi:10.2514/2.495
- [2] Cary, A. M., and Hefner, J. N., "Film-Cooling Effectiveness and Skin Friction in Hypersonic Turbulent Flow," *AIAA Journal*, Vol. 10, No. 9, 1972, pp. 1188–1193. doi:10.2514/3.50348
- [3] Sahoo, N., Kulkarni, V., Saravanan, S., Jagadeesh, G., and Reddy, K. P. J., "Film Cooling Effectiveness on a Large Angle Blunt Cone Flying at Hypersonic Speed," *Physics of Fluids*, Vol. 17, No. 3, 2005, Paper 036102. doi:10.1063/1.1862261
- [4] Marvin, J. G., and Akin, C. M., "Combined Effects of Mass Addition and Nose Bluntness on Boundary-Layer Transition," *AIAA Journal*, Vol. 8, No. 5, 1970, pp. 857–863. doi:10.2514/3.5778
- [5] Egorov, I., Vasilevskii, E., Novikov, A., and Ezhov, I., "Tangential Blowing to a Supersonic Flow on a Blunted Nose," *53rd AIAA Aerospace Sciences Meeting*, AIAA Paper 2015-0212, 2015, doi:10.2514/6.2015-0212
- [6] Barth, J. E., Wheatley, V., and Smart, M. K., "Hypersonic Turbulent Boundary-Layer Fuel Injection and Combustion: Skin-Friction Reduction Mechanisms," *AIAA Journal*, Vol. 51, No. 9, 2013, pp. 2147–2157. doi:10.2514/1.J052041
- [7] Ogorodnikov, D. A., Grin, V. T., and Zakharov, N. N., "Controlling the Boundary Layer in Hypersonic Air Intakes," *1st International Symposium on Air-Breathing Engines*, Foreign Technology Division No. FTD-HT-23-1349-72, Wright-Patterson AFB, OH, 1972.

- [8] Berry, S. A., Auslender, A. H., Dilley, A. D., and Calleja, J. F., "Hypersonic Boundary-Layer Trip Development for Hyper-X," *Journal of Spacecraft and Rockets*, Vol. 38, No. 6, 2001, pp. 853–864. doi:10.2514/2.3775
- [9] Gehre, R. M., Wheatley, V., and Boyce, R. R., "Combustion Regimes in Inlet-Fueled, Low Compression Scramjets," *20th AIAA International Space Planes and Hypersonic Systems and Technologies Conference*, AIAA Paper 2015-3507, 2015, doi:10.2514/6.2015-3507
- [10] Barth, J. E., Wise, D. J., Wheatley, V., and Smart, M. K., "Tailored Fuel Injection for Performance Enhancement in a Mach 12 Scramjet Engine," *20th AIAA International Space Planes and Hypersonic Systems and Technologies Conference*, AIAA Paper 2015-3614, 2015, doi:10.2514/6.2015-3614
- [11] Schneider, S. P., "Hypersonic Boundary-Layer Transition with Ablation and Blowing," *Journal of Spacecraft and Rockets*, Vol. 47, No. 2, 2010, pp. 225–237. doi:10.2514/1.43926
- [12] Li, F., Choudhari, M., Chang, C.-L., and White, J., "Effects of Injection on the Instability of Boundary Layers over Hypersonic Configurations," *Physics of Fluids*, Vol. 25, No. 10, 2013, Paper 104107.
- [13] Schmidt, B. E., Bitter, N. P., Hornung, H. G., and Shepherd, J. E., "Injection into Supersonic Boundary Layers," *AIAA Journal*, Vol. 54, No. 1, 2016, pp. 161–173. doi:10.2514/1.J054123
- [14] Ogawa, H., Capra, B., and Lorrain, P., "Numerical Investigation of Upstream Fuel Injection Through Porous Media for Scramjet Engines via Surrogate-Assisted Evolutionary Algorithms," *53rd AIAA Aerospace Sciences Meeting*, AIAA Paper 2015-0884, 2015, doi:10.2514/6.2015-0884
- [15] Schmidt, B. E., "On the Stability of Supersonic Boundary Layers with Injection," Ph.D. Thesis, California Inst. of Technology, Pasadena, CA, 2016, doi:10.7907/Z93X84M6
- [16] Parziale, N. J., Damazo, J. S., Schmidt, B. E., Wang, P. S., Hornung, H. G., and Shepherd, J. E., "Pulsed Laser Diode for Use as a Light Source for Short-Exposure, High-Frame-Rate Flow Visualization," *AIAA SciTech 2015*, AIAA Paper 2015-0530, 2015, doi:10.2514/6.2015-0530
- [17] Laurence, S. J., Wagner, A., Hanneman, K., Wartemann, V., Ludeke, H., Tanno, H., and Ito, K., "Time-Resolved Visualization of Instability Waves in a Hypersonic Boundary Layer," *AIAA Journal*, Vol. 50, No. 1, 2012, pp. 243–246. doi:10.2514/1.J051112
- [18] Laurence, S. J., Wagner, A., and Hanneman, K., "Schlieren-Based Techniques for Investigating Instability Development and Transition in a Hypersonic Boundary Layer," *Experiments in Fluids*, Vol. 55, No. 8, 2014, p. 1782. doi:10.1007/s00348-014-1782-9
- [19] Kennedy, R. E., Laurence, S. J., Smith, M. S., and Marineau, E. C., "Investigation of the Second-Mode Instability at Mach 14 Using Calibrated Schlieren," *Journal of Fluid Mechanics*, Vol. 845, April 2018, Paper R2. doi:10.1017/jfm.2018.269
- [20] Pappas, C. C., and Okuno, A., "Measurements of Skin Friction of the Compressible Turbulent Boundary Layer on a Cone with Foreign Gas Injection," *Journal of the AeroSpace Sciences*, Vol. 27, No. 5, 1960, pp. 321–333. doi:10.2514/8.8533
- [21] Weller, H. G., Tabor, G., Jasak, H., and Fureby, C., "A Tensorial Approach to Computational Continuum Mechanics Using Object-Oriented Techniques," *Computers in Physics*, Vol. 12, No. 6, 1998, pp. 620–631. doi:10.1063/1.168744
- [22] Arisman, C., Johansen, C. T., Bathel, B., and Danehy, P., "Investigation of Gas Seeding for Planar Laser-Induced Fluorescence in Hypersonic Boundary Layers," *AIAA Journal*, Vol. 53, No. 12, 2015, pp. 3637–3651. doi:10.2514/1.J053892
- [23] Greenshields, C. J., Weller, H. G., Gasparini, L., and Reese, J. M., "Implementation of Semi-Discrete, Non-Staggered Central Schemes in a Colocated, Polyhedral, Finite Volume Framework, for High-Speed Viscous Flows," *International Journal for Numerical Methods in Fluids*, Vol. 63, No. 1, 2009, pp. 1–21. doi:10.1002/ld.2069
- [24] Brown, G. L., and Roshko, A., "On Density Effects and Large Structure in Turbulent Mixing Layers," *Journal of Fluid Mechanics*, Vol. 64, No. 4, 1974, pp. 775–816. doi:10.1017/S002211207400190X
- [25] Mahesh, K., "The Interaction of Jets with Crossflow," *Annual Review of Fluid Mechanics*, Vol. 45, No. 1, 2013, pp. 379–407. doi:10.1146/annurev-fluid-120710-101115
- [26] Fedorov, A. V., Soudakov, V. G., and Leyva, I. A., "Stability Analysis of High-Speed Boundary-Layer Flow with Gas Injection," *AIAA 7th Theoretical Fluid Mechanics Conference*, AIAA Paper 2014-2498, 2014, doi:10.2514/6.2014-2498
- [27] Mack, L. M., "Boundary-Layer Linear Stability Theory," Jet Propulsion Laboratory and California Institute of Technology, Tech. Rept. AD-P004 046, Pasadena, CA, 1984.
- [28] Papamoschou, D., "Experimental Investigation of Heterogeneous Compressible Shear Layers," Ph.D. Thesis, California Inst. of Technology, Pasadena, CA, 1987.
- [29] Papamoschou, D., and Roshko, A., "The Compressible Turbulent Shear Layer: An Experimental Study," *Journal of Fluid Mechanics*, Vol. 197, No. 1, 1988, pp. 453–477. doi:10.1017/S0022112088003325
- [30] Dimotakis, P. E., and Brown, G. L., "The Mixing Layer at High Reynolds Number: Large-Structure Dynamics and Entrainment," *Journal of Fluid Mechanics*, Vol. 78, No. 3, 1976, pp. 535–560. doi:10.1017/S0022112076002590
- [31] Papamoschou, D., and Roshko, A., "Observations of Supersonic Free Shear Layers," *Sadhana*, Vol. 12, Nos. 1–2, 1988, pp. 1–14. doi:10.1007/BF02745657
- [32] Papamoschou, D., "Structure of the Compressible Turbulent Shear Layer," *27th AIAA Aerospace Sciences Meeting*, AIAA Paper 1989-0126, 1989, doi:10.2514/3.59935
- [33] Michalke, A., "On Spatially Growing Disturbances in an Inviscid Shear Layer," *Journal of Fluid Mechanics*, Vol. 23, No. 3, 1965, pp. 521–544. doi:10.1017/S0022112065001520
- [34] Dimotakis, P. E., "Turbulent Free Shear Layer Mixing and Combustion," *High Speed Flight Propulsion Systems*, Vol. 137, Progress in Astronautics and Aeronautics, 1991, pp. 265–340, Chap. 5.
- [35] Mehta, R. D., and Westphal, R. V., "Near-Field Turbulence Properties of Single- and Two-Stream Plane Mixing Layers," *Experiments in Fluids*, Vol. 4, No. 5, 1986, pp. 257–266. doi:10.1007/BF00369117
- [36] Pappas, C. C., and Okuno, A., "Heat-Transfer Measurement for Binary Gas Laminar Boundary Layers with High Rates of Injection," NASA TN-D-2473, 1964.
- [37] Sandham, N., and Reynolds, W., "3-Dimensional Simulations of Large Eddies in the Compressible Mixing Layer," *Journal of Fluid Mechanics*, Vol. 224, March 1991, pp. 133–158. doi:10.1017/S0022112091001684
- [38] Clemens, N., and Mungal, M., "2-Dimensional and 3-Dimensional Effects in the Supersonic Mixing Layer," *AIAA Journal*, Vol. 30, No. 4, 1992, pp. 973–981. doi:10.2514/3.11016
- [39] Zhuang, M., Dimotakis, P. E., and Kubota, T., "The Effect of Walls on a Spatially Growing Supersonic Shear Layer," *Physics of Fluids*, Vol. 2, No. 4, 1990, pp. 599–604. doi:10.1063/1.857760

M. M. Choudhari
Associate Editor